Mechanism of strong visible light photocatalysis by Ag_2O-nanoparticle-decorated monoclinic TiO_2(B) porous nanorods

Mechanism of strong visible light photocatalysis by Ag₂O-nanoparticle-decorated monoclinic TiO₂(B) porous nanorods

Kamal Kumar Paul[1], Ramesh Ghosh[1] and P K Giri[1,2]

[1] Department of Physics, Indian Institute of Technology Guwahati, Guwahati-781039, India
[2] Centre for Nanotechnology, Indian Institute of Technology Guwahati, Guwahati-781039, India

E-mail: giri@iitg.ernet.in

Abstract

We report on the ultra-high rate of photodegradation of organic dyes under visible light illumination on Ag₂O-nanoparticle-decorated (NP) porous pure B-phase TiO₂ (TiO₂(B)) nanorods (NRs) grown by a solvothermal route. The as-grown TiO₂(B) NRs are found to be nanoporous in nature and the Ag₂O NPs are uniformly decorated over its surface, since most of the pores work as nucleation sites for the growth of Ag₂O NPs. The effective band gap of the TiO₂(B)/Ag₂O heterostructure (HS), with a weight ratio of 1:1, has been significantly reduced to 1.68 eV from the pure TiO₂(B) band gap of 2.8 eV. Steady state and time-resolved photoluminescence (PL) studies show the reduced intensity of visible PL and slower recombination dynamics in the HS samples. The photocatalytic degradation efficiency of the TiO₂(B)/Ag₂O HS has been investigated using aqueous methyl orange and methylene blue as reference dyes under visible light (390–800 nm) irradiation. It is found that photodegradation by the TiO₂(B)/Ag₂O HS is about one order of magnitude higher than that of bare TiO₂(B) NRs and Ag₂O NPs. The optimized TiO₂(B)/Ag₂O HS exhibited the highest photocatalytic efficiency, with 88.2% degradation for 30 min irradiation. The corresponding first order degradation rate constant is $0.071\ \mathrm{min}^{-1}$, which is four times higher than the reported values. Furthermore, cyclic stability studies show the high stability of the HS photocatalyst for up to four cycles of use. The major improvement in photocatalytic efficiency has been explained on the basis of enhanced visible light absorption and band-bending-induced efficient charge separation in the HS. Our results demonstrate the long-term stability and superiority of the TiO₂(B)/Ag₂O HS over the bare TiO₂(B) NRs and other TiO₂-based photocatalysts for its cutting edge application in hydrogen production and environmental cleaning driven by solar light photocatalysis.

S Online supplementary data available from stacks.iop.org/NANO/27/315703/mmedia

Keywords: visible light photocatalysis, TiO₂(B)/Ag₂O heterostructure, photoluminescence lifetime

(Some figures may appear in colour only in the online journal)

1. Introduction

Photocatalysis by metal oxide semiconductors is being studied extensively due to its potential application in clean hydrogen energy production and environmental protection such as waste-water treatment, water splitting, CO₂ reduction, air purification, disinfection and self-cleaning surfaces [1–4]. In comparison to other semiconductors, TiO₂ is one of the

most suitable and promising semiconductor photocatalysts because of its high chemical stability, low cost, non-toxicity, high oxidizing power and good degradation efficiency [5–7]. However, a major limitation of TiO_2 is that it has a large band gap (3.2 eV for the anatase phase and 3.0 eV for the rutile phase) and can only utilize the UV light (wavelength <400 nm) from the whole solar spectrum, limiting its application in the industry, which requires maximum utilization of the visible and near infrared (NIR) region of the solar spectrum. In addition, the high recombination rate of the photo-generated electron–hole pairs prevents their migration to the surface of semiconductor photocatalysts causing low photo-catalytic efficiency [8, 9]. When TiO_2 absorbs UV photons, active electrons and holes are created and these electrons and holes need to migrate to the surface to initiate a redox reaction. In a homogeneous semiconductor, the recombination of the photoexcited electrons and holes simply by liberating heat (non-radiative transition) or light (radiative transition) is highly probable, which results in the low quantum yield of the reaction [10, 11]. Several strategies have been proposed for enhancing the charge separation and the light absorption in TiO_2 in the visible region. This has been achieved by the formation of heterostructures (HSs) through metallization [11–18], sensitization [8, 19–21]), impurity doping [22–24], defect engineering [25–27] etc. By decorating them with noble metal NPs such as Ag, Cu, Au, Pt, Pd etc, the photo-catalytic efficiency of a semiconductor photocatalyst can be enhanced, as the noble metal NPs act as an electron acceptor elevating the interfacial charge transfer of the HS [12–14, 28]. Furthermore, reutilization of the powder photocatalyst is still a big challenge. Nano-sized catalyst particles are usually hard to recover from large volumes of photocatalysis chambers, as the NPs (e.g. P-25) make a highly stable suspension in water [29]. TiO_2 photocatalysts of a larger size (∼a few μm) usually segregate and can be used successfully for multiple cycles. Very few groups have reported on the visible light sensitization of TiO_2 nanostructures by decorating them with Ag_2O NPs [8, 30]. Although $TiO_2(B)/Ag_2O$ HSs exhibit higher visible light absorption and improved visible light photo-catalytic efficiency, they require further investigation in order to achieve higher visible light absorption, and faster inter-facial charge transfer, leading to a prolonged charge carrier lifetime and resulting in superior visible light photocatalytic activity. To our knowledge, the $TiO_2(B)$ phase and its HS with Ag_2O NPs have not been explored yet for the visible light photocatalysis of organic dyes. The $TiO_2(B)$ phase is a less compact structure than that of other forms of TiO_2. The volume of a TiO_2 unit in $TiO_2(B)$ is 35.27 Å^3 as compared to that of 31.12 Å^3 for rutile, 32.20 Å^3 for brookite and 34.02 Å^3 for anatase phases.

Here, we have grown porous 1D $TiO_2(B)$ nanorods (NRs) by a basic ethylene-glycol-mediated solvothermal method. The Ag_2O NPs are decorated uniformly on the surface of the $TiO_2(B)$ NRs by a simple co-precipitation method. The $TiO_2(B)$ NRs are expected to possess certain advantages over TiO_2 NPs owing to their higher aspect ratio, higher visible light absorption, very few grain boundaries and diffusion-free fast electron transport along the length of the NR.

The effective band gap of the as-grown $TiO_2(B)/Ag_2O$ HS has been tuned here to absorb strongly in the entire visible region. The HS shows huge amounts of visible light absorption extending up to the NIR region of the solar spectrum. The photocatalytic activity of the $TiO_2(B)/Ag_2O$ composite has been investigated using aqueous methyl orange (MO) and methylene blue (MB) as reference dyes under visible light irradiation. We report on the massive (∼13 times) enhancement in the photocatalytic rate constant of the $TiO_2(B)/Ag_2O$ HS by incorporating the low band gap Ag_2O NPs as photosensitizers. Steady state and time-resolved photoluminescence (PL) analyses of the samples have been performed to understand the mechanism of superior photo-catalytic performance. Our results show the superiority of the $TiO_2(B)/Ag_2O$ HS over the bare $TiO_2(B)$ NRs and other TiO_2-based HSs for environmental cleaning applications.

2. Experimental procedure

2.1. Preparation of porous $TiO_2(B)$ NRs

$TiO_2(B)$ NRs were synthesized using a typical solvothermal process in a concentrated NaOH solution of DI water and ethylene glycol in a 1:1 volume ratio. In a typical synthesis, 1 g of precursor anatase TiO_2 powder (Merck, average particle size ∼80 nm) was mixed with 48 ml of 10 M NaOH mixed solvent (DI water : ethylene glycol = 1:1) under stirring for 1 h, followed by hydrothermal treatment in a 100 ml Teflon-lined autoclave (Berghof, BR-100). The temperature inside the autoclave chamber was measured and maintained at 180 °C under autogenous pressure and constant magnetic stirring at 500 rpm for 16 h. The formed precipitates were washed thoroughly with DI water and obtained by centrifugation followed by a drying process at 80 °C. The obtained sodium titanate NRs were treated ultrasonically with 0.1 N HCl until the pH had nearly reduced to 7, and the precipitates were subsequently washed several times with DI water to obtain hydrogen titanate NRs. Then, the H-titanate NRs were calcined at 500 °C for 5 h in air to grow porous $TiO_2(B)$ NRs.

2.2. Growth of $TiO_2(B)/Ag_2O$ NR heterostructures

$TiO_2(B)/Ag_2O$ HSs with various weight ratios from 1:3 to 3:1 were synthesized by a precipitation method. Typically for a 1:1 weight ratio, 0.1 g of the $TiO_2(B)$ NRs was dispersed in 50 ml of DI water and then 0.145 g of $AgNO_3$ was dissolved into the above suspended solution. Said mixture was then stirred magnetically for 30 min to reach adsorption equilibrium. Next, 50 ml of 0.2 M aqueous NaOH solution was added drop-wise to the mixture. The amount of NaOH was enough to form a precipitation of Ag_2O NPs from the $AgNO_3$. During this process, the Ag_2O NPs were coated on the $TiO_2(B)$ NRs and the final pH of the solution was measured to be 14. The $TiO_2(B)/Ag_2O$ HS was obtained by washing with DI water several times, filtration and drying. Pure Ag_2O NPs were also synthesized as a blank material for comparison. In

Table 1. Sample specifications, optical absorption range and effective band gap of different HS samples.

HS sample specifications		Sample code	Absorption region	Effective band gap (eV)
Weight ratio of				
TiO_2	Ag_2O			
1	0	TiO_2(B)	UV	2.80
2	1	TA1	UV–vis–NIR	2.20
1	1	TA2	UV–vis–NIR	1.68
1	2	TA3	UV–vis–NIR	2.03
0	1	Ag_2O	UV–vis–NIR	1.34

this case, 0.85 g of $AgNO_3$ was dissolved in 50 ml of DI water and 50 ml of 0.05 M aqueous NaOH solution was dropped into the above solution. A summary of the samples studied with the sample codes is provided in table 1.

2.3. Characterization techniques

The crystal structure of the as-grown catalysts was obtained from an x-ray powder diffraction (XRD) pattern (Rigaku RINT 2500 TTRAX-III, Cu kα radiation). The crystallinity and phase composition of the as-synthesized NRs and NPs were measured by micro-Raman spectroscopy (LabRam HR800, Jobin Yvon). The morphology, size and the elemental compositions of the as-synthesized TiO_2(B) NRs and the TiO_2(B)/Ag_2O HS were studied using a field emission scanning electron microscope (FESEM) (Sigma, Zeiss) equipped with an energy dispersive x-ray (EDX) spectrometer. The high magnification surface morphologies and structures of the as-grown samples were studied using a transmission electron microscope (TEM) (JEOL-JEM 2010 operated at 200 kV). The samples for TEM analysis were prepared on a carbon-coated Cu grid of 400 meshes (Pacific Grid, USA). UV–vis diffuse reflectance spectroscopy (DRS) measurements of the samples were recorded using a commercial spectrophotometer (PerkinElmer, UV win Lab). X-ray photoelectron spectroscopy (XPS) was carried out using a PHI X-tool automated photoelectron spectrometer (ULVAC-PHI, Japan) with an Al Kα x-ray beam (1486.6 eV) at a beam current of 20 mA. The shift in the binding energy of various catalysts was corrected using a C1s spectrum at 284.8 eV as a standard value [31]. The room temperature steady state photoluminescence (PL) spectra were recorded using a 405 nm diode laser excitation with the help of a single grating monochromator (Triax 550) and a cooled CCD detector (Jovin Yvon). Each spectrum was corrected for detector response after background subtraction. Time-resolved photoluminescence (TRPL) spectra were recorded using a picosecond time-resolved luminescence spectrometer (Edinburgh Instruments, model: FSP920). Nitrogen adsorption–desorption isotherms were conducted using a Quanta-chrome autsorb-iQ MP analyzer at 77 K. The surface area of the catalysts was determined using the multipoint Brunauer–

Emmett–Teller (BET) method and the average pore size determined using the Barett–Joyner–Halenda (BJH) model. The photocatalytic activity of the synthesized photocatalysts was studied using a time-programmable commercial photochemical reactor (Lelesil Innovative Systems, Mumbai), with a visible lamp source.

2.4. Photocatalytic degradation under visible light

The photocatalytic activity of the pure TiO_2(B) NRs and the TiO_2(B)/Ag_2O HS were evaluated considering the photodegradation of methyl orange (MO) and methylene blue (MB) as model dyes under visible light irradiation. In a typical experiment, 100 ml aqueous suspension of MO/MB (10 mg l^{-1}) and 20 mg of catalyst powders were placed in a 250 ml beaker. Before visible light irradiation, the mixture of dye solution and photocatalyst were magnetically stirred in the dark for 30 min. This allowed the establishment of the adsorption–desorption equilibrium between the interface of the photocatalysts and dye molecules under ambient conditions. A 250 W lamp with an emission in the range 390–800 nm was used as the light source for the visible light photocatalysis. The lamp is surrounded by a water-cooled quartz jacket that absorbs the heat generated from the high-power lamp. This maintains the constant temperature of the whole environment and it ensures that degradation only occurs because of light irradiation and not heat. At chosen irradiation intervals, 5 ml of solution was collected and centrifuged to remove the catalyst particles for further study. In order to estimate the residual concentration of the dye solution, the UV–vis absorbance was measured in a Shimadzu 2450 UV–vis spectrophotometer.

3. Results and discussions

3.1. Morphology studies

The growth of TiO_2 NRs by the solvothermal process as well as Ag_2O NP decoration on the NRs have been discussed by several groups [8, 32]. It has been recognized that during the growth process, porous-like TiO_2 NRs are formed under certain conditions. In order to understand the morphology and microstructural properties of the as-synthesized TiO_2 NRs, Ag_2O NPs and their HSs, we performed an FESEM analysis of the samples. Figure 1(a) shows the FESEM image of pure TiO_2 NRs with a diameter of ~40–180 nm and lengths of up to a few micrometers, while figure 1(b) shows the FESEM image of a TiO_2(B)/Ag_2O HS (named TA2, see table 1). Since the size of the as-grown Ag_2O NPs is very small (~5.3 nm, as revealed by the TEM analysis), even in the presence of the Ag_2O NPs, the surface of the TiO_2 NRs seems to be smooth in the FESEM image. EDX analysis on the as-grown TiO_2 NRs reveals that (see figure 1(c)) it is only composed of Ti and O elements with a 1:2.24 atomic ratio. The EDX analysis of sample TA2 in figure 1(d) confirms that the HS consists of Ti, Ag and O elements. Figure 1(e) shows the FESEM image of the bare Ag_2O NPs. The size of the
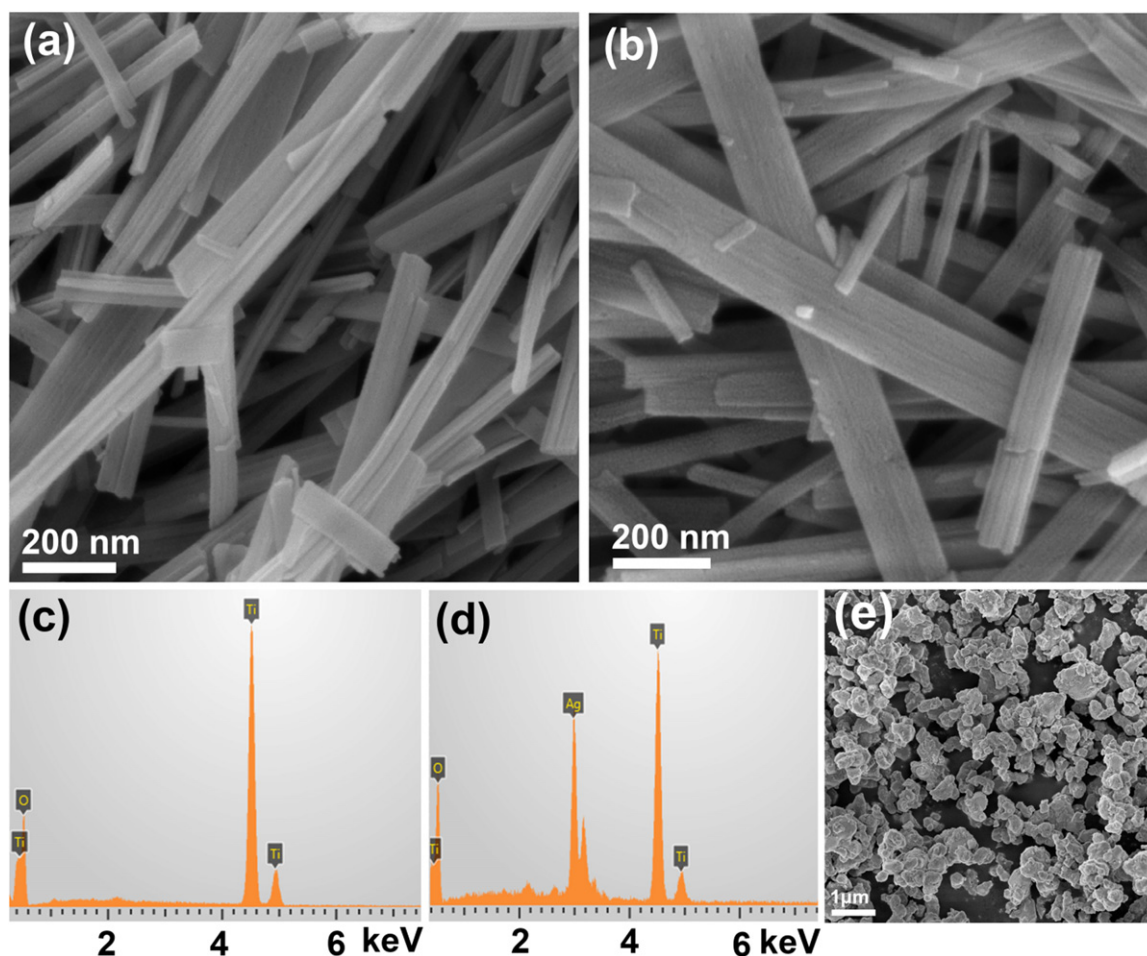
Figure 1. FESEM images of the TiO$_2$ NRs: (a) before, (b) after Ag$_2$O NP decoration. (c) and (d) The corresponding EDX spectra. (e) FESEM images of bare Ag$_2$O NPs.

Ag$_2$O NPs varies from 100–600 nm, which is much larger than the NPs decorated on the TiO$_2$ NR surface. In the case of Ag$_2$O NPs on the surface of the TiO$_2$ NRs, the presence of numerous small pores on the surface of the latter serve as nucleation sites for the growth of small Ag$_2$O NPs, which minimizes the probability of aggregation.

To investigate the high resolution surface features of the NRs, TEM images are acquired for the respective samples that confirm the nanoporous nature of the TiO$_2$ NR and its HS with the Ag$_2$O NPs. Figure 2(a) shows the TEM image of a TiO$_2$ NR, while figure 2(b) depicts the TEM image of sample TA2. It is clear from figure 2(a) that the surface of the TiO$_2$ NR is rough in nature and this is due to the presence of uniformly distributed pores on the NR. Note that the porous regions are primarily the nucleation and growth sites for the Ag$_2$O NPs grown by the precipitation method. The pores on the surface of the TiO$_2$ NR provide a noble stage on which to grow Ag$_2$O NPs, which are strongly attached to the TiO$_2$ NRs. Figure 2(b) confirms that the Ag$_2$O NPs are quite uniformly distributed on the surface of the TiO$_2$ NRs, though some regions without the NPs still show ultrafine pores on them. The pores on the pristine TiO$_2$ NRs have an average diameter of ∼6.8 nm (shown in figure 2(c)) and the decorated Ag$_2$O NPs have an average diameter of ∼5.3 nm (shown in figure 2(d)). As the

pores are uniformly distributed across the surface of the TiO$_2$ NRs, the distribution of the Ag$_2$O NPs is also nearly uniform. Due to the strong coupling, the decorated NPs are very stable on the porous surface of the TiO$_2$ NRs and do not get detached, even under strong ultrasonic vibration. Figure 2(e) shows the HRTEM lattice image of the TiO$_2$(B)/Ag$_2$O HS, which clearly reveals the simultaneous presence of crystalline Ag$_2$O and TiO$_2$(B) phases. As the Ag$_2$O NPs are tightly coupled to the TiO$_2$ NRs, efficient electron transport is expected at the interface of the HS. The lattice spacing (d) of the TiO$_2$(B) and Ag$_2$O was calculated by measuring the intermediate distance between the lattice fringes. Pure B-phase TiO$_2$ with (110) crystal planes (d = 0.355 nm) and cubic Ag$_2$O with (200) crystal planes (d = 0.235 nm) can be confirmed from the lattice fringe image. The SAED pattern of the corresponding HS is shown in figure 2(f), which further confirms the crystalline nature of both Ag$_2$O and TiO$_2$(B). The (002) and (023) crystal planes of pure TiO$_2$(B) and (200) the crystal plane of Ag$_2$O have been indexed in figure 2(f).

3.2. Structural analysis

3.2.1. XRD and Raman analysis. In order to confirm the structure, phase and crystallinity of the as-synthesized TiO$_2$
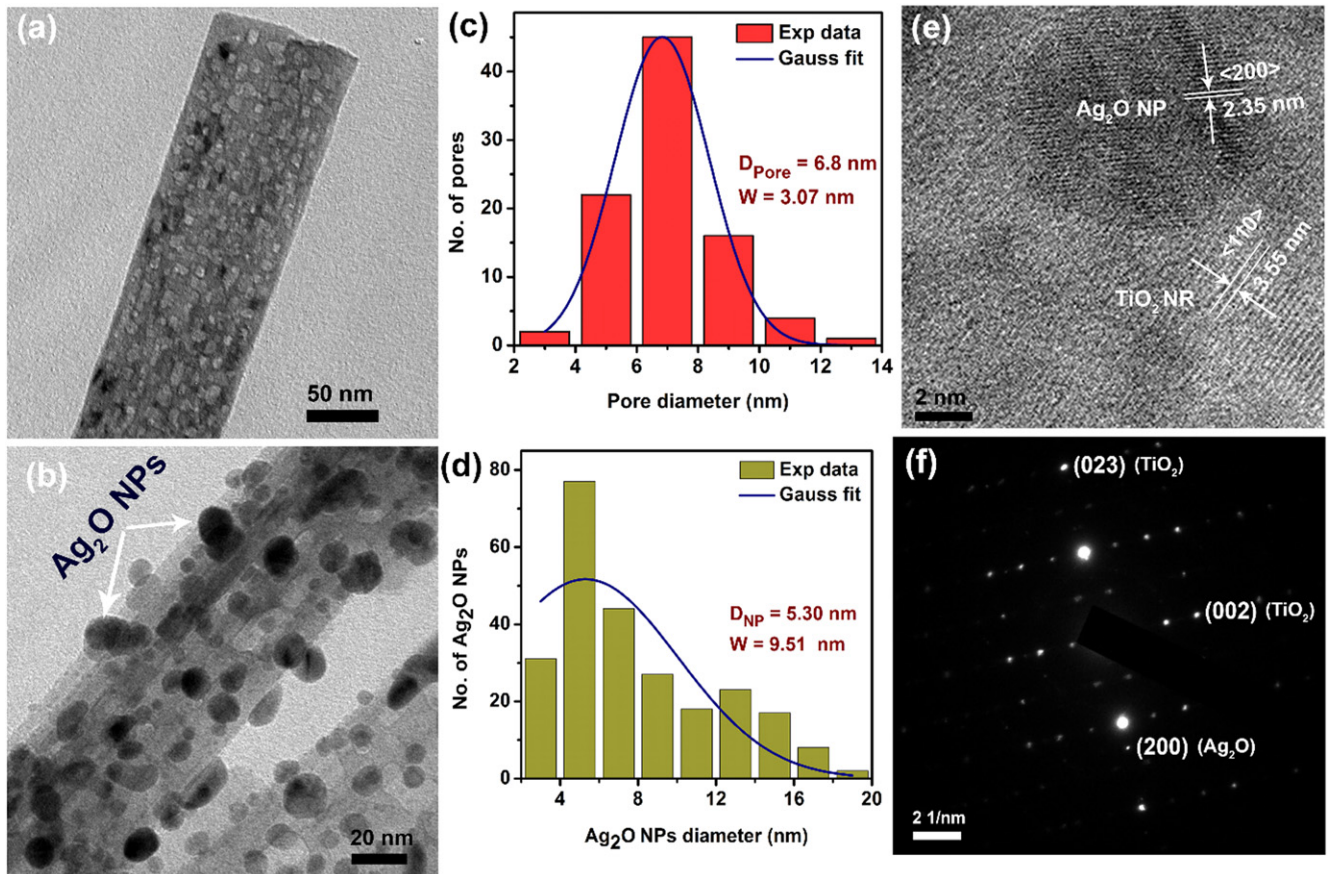
Figure 2. TEM images of: (a) a single TiO_2(B) NR with nano-sized pores on it, (b) the TiO_2(B)/Ag_2O NR HS in TA2. (c) The distribution of the pore diameter on TiO_2(B) NRs, and (d) the diameter distribution of Ag_2O NPs on TiO_2(B) NRs and their Gaussian fitting. The average diameter (*D*) and width of the distribution (*W*) are also shown in the respective cases. (e) The HRTEM lattice fringe image of TA2. The lattice spacing of Ag_2O and TiO_2(B) with its orientation is also shown. (f) The SAED pattern of TA2 indicating the different planes of Ag_2O as well as TiO_2(B).

NRs, Ag_2O NPs and their HSs, XRD patterns of each sample were recorded, as shown in figure 3. Each diffraction peak of the TiO_2 NRs corresponds to a pure TiO_2(B) phase [32] with a monoclinic structure and that of the Ag_2O NPs corresponds to the cubic structure [8]. The peaks corresponding to the TiO_2(B) phase are marked by red diamonds, while those of the cubic Ag_2O are marked by black circles (filled). The diffraction peaks of the Ag_2O NPs are sharp, clearly implying that Ag_2O NPs are highly crystalline in comparison to the pristine TiO_2(B) and TA2. The phases of TiO_2(B) and Ag_2O co-exist in the TiO_2(B)/Ag_2O HS sample. Note that the XRD analysis on the HS sample does not show any measurable change in the crystal structure or the lattice parameter of the TiO_2(B) NRs. However, the XRD data does show a slight downshift in the Ag_2O peaks in the HS sample as compared to the pristine Ag_2O NPs, as shown in figure S1 (supporting information). This implies a tensile strain in the Ag_2O NPs in the HS due to the strong coupling between the TiO_2(B) and the Ag_2O lattice, which is fully consistent with the Raman and XPS results discussed later.

For further endorsement of the crystalline nature and phase of the TiO_2 NR and its HS, Raman analysis was
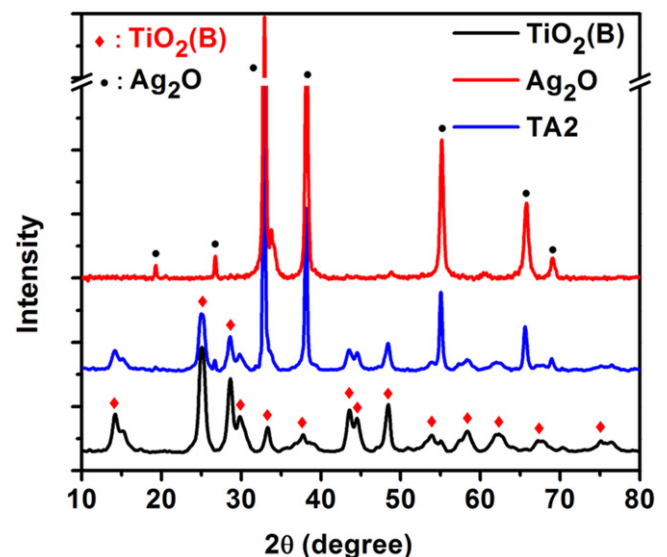

Figure 3. XRD patterns of TiO_2(B) NRs, Ag_2O NPs and the TA2 HS. The curves are vertically shifted for clarity of presentation. The peaks corresponding to TiO_2(B) are indicated by red diamonds and the same for Ag_2O as black circles (filled).

performed for all the samples using a 633 nm laser excitation. Figure S2 (supporting information) shows a comparison of the Raman spectra for all the samples. The inset shows a magnified view of the prominent Raman modes in the region 250–1000 cm^{-1}. The peaks corresponding to the B-phase of the TiO$_2$ are marked '∗', while those of the Ag$_2$O are marked '♦' [32]. Note that the peak intensities of the HS samples gradually decrease with an increase in Ag$_2$O loading. The crystalline Ag$_2$O peaks at 323 and 489 cm^{-1} correspond to the Ag–O stretching/bending modes [33].

3.2.2. XPS analysis. To investigate the chemical environment, the elemental composition and the surface defects on the nanostructures, XPS studies were carried out. Figure 4(a) shows a comparison of the Ag 3d core level spectra of the Ag$_2$O NPs and the TiO$_2$(B)/Ag$_2$O HS (TA2). Both the samples show a single valence Ag$^+$ state in Ag$_2$O corresponding to a Ag 3d$_{5/2}$ peak at ∼367.9 eV [34]. Note that in the TiO$_2$(B)/Ag$_2$O HS, the Ag 3d$_{5/2}$ peak is slightly red-shifted to the lower binding energy as compared to that in bare Ag$_2$O NPs. A vertical dotted line is drawn at 367.9 eV to discern the red shift. The fittings of the spectra for Ag$_2$O and TA2 with an appropriate baseline (Shirley) are shown in figures 4(b) and (c), respectively. In the case of the TA2 HS, each of the 3d peaks fit a single peak corresponding to the Ag$^+$ state. Details of the fitting parameters are presented in table T1 (supporting information). The shift in the peak could have resulted from the strong interaction of Ag$_2$O with the TiO$_2$(B) NRs and may also have resulted from the strain in the Ag$_2$O NPs that had been grown on the porous TiO$_2$(B) surface. Note that the atomic ratio of Ag to O found by XPS analysis is 2.1:1, indicating that no other phases of Ag oxides are present in the sample. Figure 4(d) shows a comparison of the XPS core level Ti 2p spectra of the TiO$_2$(B) NRs before and after Ag$_2$O loading. A Ti 2p$_{3/2}$ peak for TiO$_2$ NRs was found at 458.6 eV, and is assigned to the Ti^{4+} valence state confirming the formation of TiO$_2$ [32]. However, after the decoration of Ag$_2$O NPs on the TiO$_2$(B) NRs, the Ti 2p$_{3/2}$ peak was slightly red-shifted to a lower binding energy of 458.2 eV (as indicated by the vertical dotted line). This shift in the Ti 2p$_{3/2}$ peak of the TiO$_2$(B)/Ag$_2$O HSs may have been due to the lattice distortion induced in the TiO$_2$(B) due to strong coupling between the TiO$_2$(B) lattice with the Ag$_2$O NPs [35]. This may partly be due to band bending at the TiO$_2$/Ag$_2$O interface. Figures 4(e) and (f) show the deconvolution of the XPS spectra for the bare TiO$_2$ and TA2 HS. Altogether, four peaks are fitted to the spectrum in each case. Peak 1 and peak 3 correspond to the Ti^{3+} state, and peak 2 and peak 4 correspond to the Ti^{4+} state. A summary of the fitting parameters is shown in table T1 (supporting information). It may be noted that the relative intensity of peak 1 is reduced in TA2 as compared to that of bare TiO$_2$(B) and this could be due to the reduction of oxygen vacancy defects. This is fully consistent with the PL analysis that shows lower vacancy concentration in TA2, as discussed later. Thus, the XPS results show strong coupling between the Ag$_2$O NPs and TiO$_2$(B) NRs in the HS samples, and this plays an important role in the enhanced photocatalytic efficiency.

3.3. Brunauer–Emmett–Teller (BET) surface area analysis

In order to assess the specific surface area of the nanoporous TiO$_2$(B) NR, its HS, and the coupling between the porous sites of the TiO$_2$(B) NRs and Ag$_2$O NPs, the surface area of the samples was measured by the BET process. The N$_2$ adsorption–desorption isotherms of the TiO$_2$(B) NRs and TiO$_2$(B)/Ag$_2$O HS (TA2) are shown in figures S3(a) and (b), respectively (supporting information). The shape of the isotherms depends on the pore sizes of the nanostructure. The isotherms of the nanostructures with micropores (size ⩾1 nm) exhibit an abrupt increase in the high-pressure region (>0.8 P P$_0^{-1}$ value) that can be attributed to the capillary condensation and multilayer adsorption of N$_2$ in the micropores. Besides the pores, the TiO$_2$(B) nanostructures have rough surfaces. So, the isotherms show smooth behavior without any inflections before capillary condensation transition [36]. In this work, the surface area of the pristine TiO$_2$(B) NRs is measured as 51.09 m^2 gm^{-1}, while that of the TA2 HS is 28.6 m^2 gm^{-1}, as deduced from the BET analysis. Thus, after the loading of Ag$_2$O NPs onto the TiO$_2$(B), the surface area of the HS is considerably reduced. Note that some of the pores on the TiO$_2$(B) surface act as nucleation sites for the growth of Ag$_2$O NPs. Furthermore, the BET provides the surface area of the material per unit mass (m^2 gm^{-1}). Since the molar mass density of Ag$_2$O (7.14 gm cm^{-3}) is nearly double that of the TiO$_2$(B) (4.23 gm cm^{-3}), the surface area of the HS sample is reduced by nearly half, primarily due to Ag$_2$O loading with nearly double the molar mass density. Thus, the reduced surface area in the HS sample is mainly due to the higher mass loading effect, without any substantial reduction in average pore size. It is apparent from the HRTEM analysis that the average size of the Ag$_2$O NPs is much larger than the pore sizes measured using the Barett–Joyner–Halenda (BJH) analysis (figure S3) (supporting information). The BJH pore size distribution profiles for pristine TiO$_2$(B) and the TA2 HS are shown in figures S3(c) and (d) (supporting information). The average pore diameter is found to be ∼1.9 nm for both the samples, as determined by the distribution profile. However, this size is much less than the pore sizes obtained using the HRTEM analysis (6.8 nm), primarily due to the limitations of the TEM technique in probing ultra-small pore sizes. In the case of the HS sample, the bigger-sized pores are covered with Ag$_2$O NPs, while the smaller pores with a very high density are still uncovered, as evident from figures 2 and S3 (supporting information). Although the average surface area is reduced in the HS sample, the presence of small pores and the effect of heterojunctions dramatically improve photocatalytic efficiency in the HS.

3.4. Optical analysis

3.4.1. UV–vis absorption study. To assess optical absorbance, a DRS measurement of the samples was carried
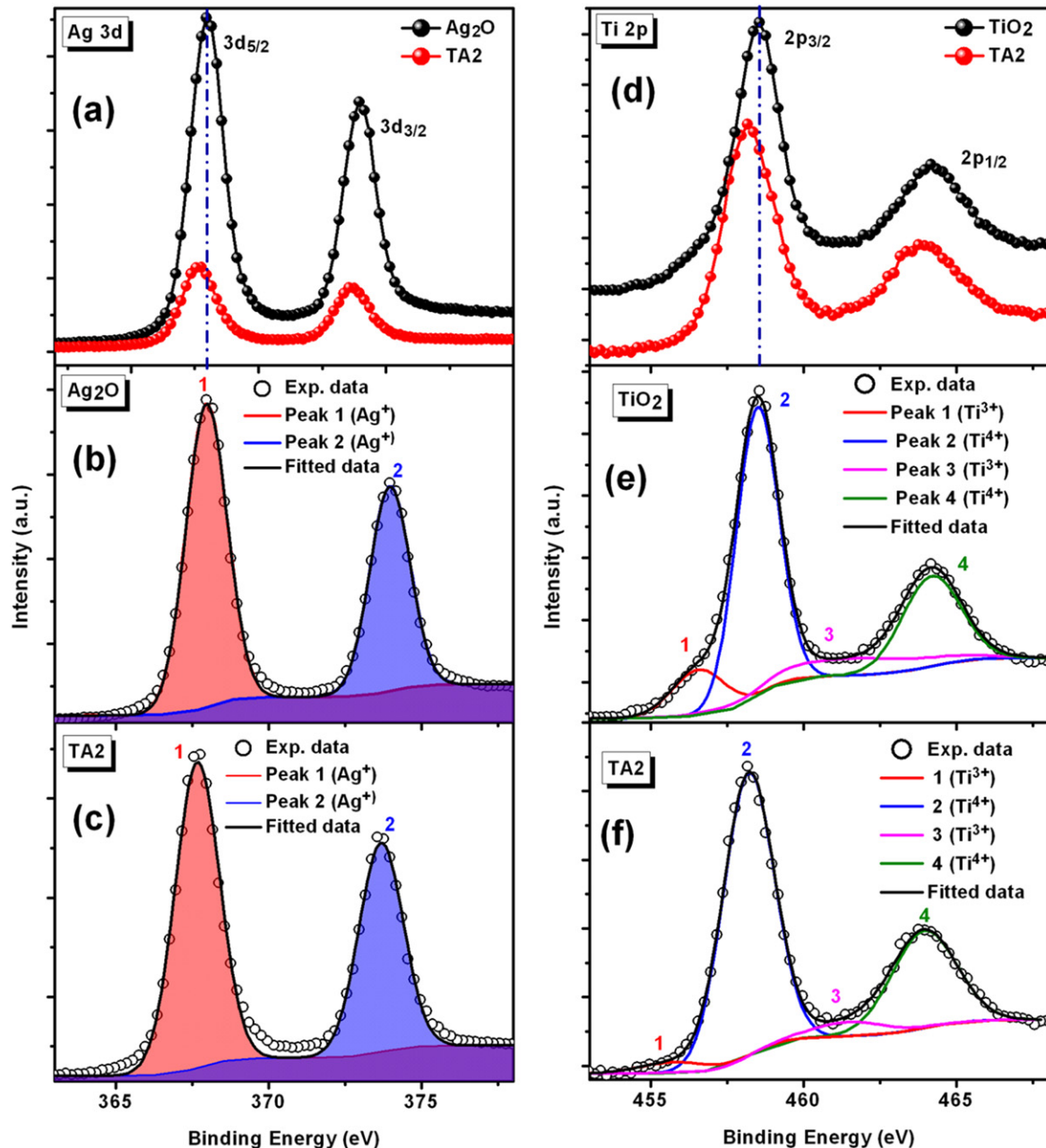
Figure 4. (a) A comparison of the core level XPS Ag 3d spectra for the Ag_2O NPs and TA2 HS. (b), (c) The fitted XPS spectra for Ag_2O and TA2, respectively, with a Shirley baseline. (d) A comparison of the core level XPS Ti 2p spectra for the bare $TiO_2(B)$ and TA2 HS. The vertical dashed-dotted lines drawn at 367.9 eV in (a) and 458.6 eV in (d) indicate a red shift in the binding energy in the case of the HS sample. (e), (f) The fitted XPS spectra for the bare $TiO_2(B)$ and TA2 HS, respectively, with a Shirley baseline. The identity of each peak is denoted by the corresponding charge states in the respective cases.

out. Figure 5(a) shows a comparison of the absorbance of various samples in the range 200–850 nm. As evident from the data, the pristine $TiO_2(B)$ NRs exhibit a sharp absorption edge at ~400 nm, and at higher wavelengths (visible region) the absorbance is negligibly low. However, the pristine Ag_2O NPs have strong absorption in the UV–visible–NIR range of 200–850 nm, showing a broad absorption band centered at ~430 nm and an absorption tail extending to the NIR region. The calculated band gap (direct) from the corresponding Tauc plot is ~1.34 eV, consistent with the literature report [37]. The absorption spectra of the $TiO_2(B)/Ag_2O$ HSs illustrate that

the HS system has extremely high absorption in the entire UV–visible–NIR region of the optical spectrum. Although each spectrum exhibits very high visible light absorption efficiency with a broad envelope covering 600–690 nm, the HS with Ag_2O and $TiO_2(B)$ in a 1:1 weight ratio shows the highest absorption in the visible to NIR region. For visible light sensitization by Ag_2O NPs, the HSs are expected to have high photocatalytic activity in the visible as well as UV and NIR region. Interestingly, the effective band gap of the $TiO_2(B)$ NRs was reduced greatly after loading with Ag_2O NPs. Considering the indirect nature of the band gap in the
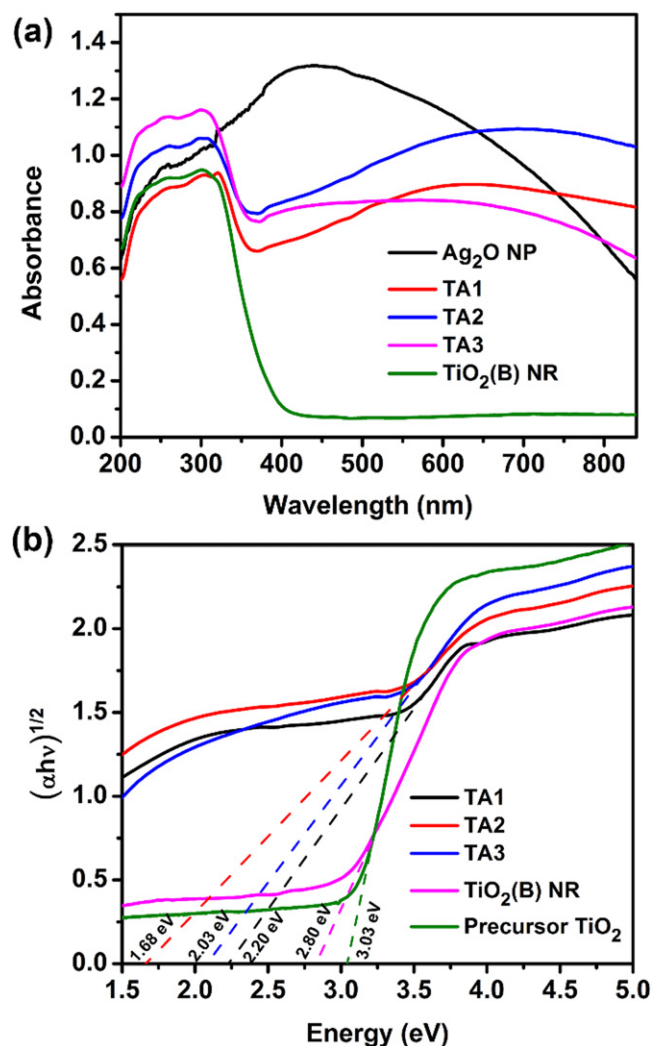
Figure 5. (a) UV–vis–NIR absorption spectra of different samples. (b) The corresponding Tauc plot considering the indirect band gap nature of the TiO_2 samples. The effective band gaps of the respective samples are estimated by the intercept on the *x*-axis (extrapolated dashed lines).

$TiO_2(B)$ NR as well as its HS, the effective band gap of the respective samples was estimated using the Tauc plot, as shown in figure 5(b) [32]. The precursor anatase TiO_2 nanopowder has a band gap of 3.03 eV, which is reduced to 2.80 eV in the case of bare $TiO_2(B)$ NRs. This reduction in the effective band gap helps the $TiO_2(B)$ NRs to be very active under visible light, and they are expected to have significant visible light photodegradation capability. The most interesting fact is that after the decoration of the Ag_2O NPs, the effective band gap energy of the $TiO_2(B)$ NRs is tuned in the range 2.20–1.68 eV and the effective band gap of the respective samples is shown in 5(b). The detailed absorption range and the effective band gap of each sample are tabulated in table 1. The band gap energy modification for the HS samples may be due to the efficient coupling between the Ag_2O NPs and $TiO_2(B)$ NRs. The band structures of each of the nanocomponents are suitable enough to have proper band bending at the interface due to their close coupling. It is

noteworthy that in case of TA2, the effective band gap is found to be the lowest (1.68 eV), which implies that Ag_2O NPs and the $TiO_2(B)$ NR HS have large band bending and may have high carrier concentrations at room temperature. This turns out to be a very promising and an extremely beneficial approach for efficient visible light photocatalysis in the HS samples (discussed later) [38].

3.4.2. Photoluminescence study. The superiority of the as-prepared HS as a solar light photocatalyst over the bare $TiO_2(B)$ NRs is confirmed by the PL studies. The characteristic PL spectra clarify the mode of separation and recombination of the photogenerated e–h pairs. A comparison of the room temperature PL spectra for the $TiO_2(B)$ NRs, Ag_2O NPs and TA2 HS is shown in figure 6(a). Interestingly, a significant decrease (by a factor of ∼5.9) in PL intensity of the $TiO_2(B)$ NRs was observed after decoration with the Ag_2O NPs. However, the center of the PL band remained unchanged. In order to understand the origin of the broad visible PL of the $TiO_2(B)$ NRs before and after Ag_2O NP loading, the PL spectrum of each sample is deconvoluted with Gaussian peaks. The deconvoluted PL spectra for the $TiO_2(B)$ NRs and TA2 are shown in figures 6(b) and (c), respectively. In each case, the spectrum is fitted well by four Gaussian bands and the individual bands are labeled as peaks 1, 2, 3 and 4. Peak 1 (at 427.2 nm) in figure 6(b) is attributed to the self-trapped excitons located in the TiO_6 octahedra [32]. Peak 2 (at 491.2 nm) is due to the charge transfer transition from the Ti 3d orbital to the O 2p orbital in the TiO_6^{2-} octahedra [39], while peak 3 (at 560.6 nm) is attributed to the shallow traps associated with the oxygen vacancies (V_O) in the TiO_2 structure [40]. Peak 4 (641.0 nm) is possibly due to the deep-level emissions associated with V_O states [41]. It is confirmed from figure 6(c) that the peak centers of the individual bands of sample TA2 are unaltered from that of the $TiO_2(B)$ NRs. Note that the intensity ratio of the peaks in each sample is also almost the same in figures 6(b) and (c). However, the intensity of each peak decreases strongly in sample TA2 as compared to that in the $TiO_2(B)$ NRs. The lowering of PL intensity after decoration with Ag_2O NPs may be due to the following reasons: (i) the deposited Ag_2O NPs work as traps for the photoexcited electrons and prevent their recombination; [8] (ii) due to band bending at the interface, the charge transfer process is very efficient in the case of the HSs, and thus the charge carriers (e, h) are separated enough to reduce recombination probability and hence the PL intensity; (iii) the Ag_2O NPs may partly passivate the luminescent centers in $TiO_2(B)$ NRs. All these factors may contribute to the decrease in the PL intensity of sample TA2 as compared to the $TiO_2(B)$ NRs. Thus, under visible light illumination, plenty of excitons are available at the interface of the $TiO_2(B)/Ag_2O$ HS, which may help in achieving high photocatalytic activity (discussed later).

3.4.3. Time-resolved photoluminescence study. To understand the carrier dynamics of recombination in the $TiO_2(B)$ NR and its HS, we studied the time-resolved PL spectra. Figure 7 shows a
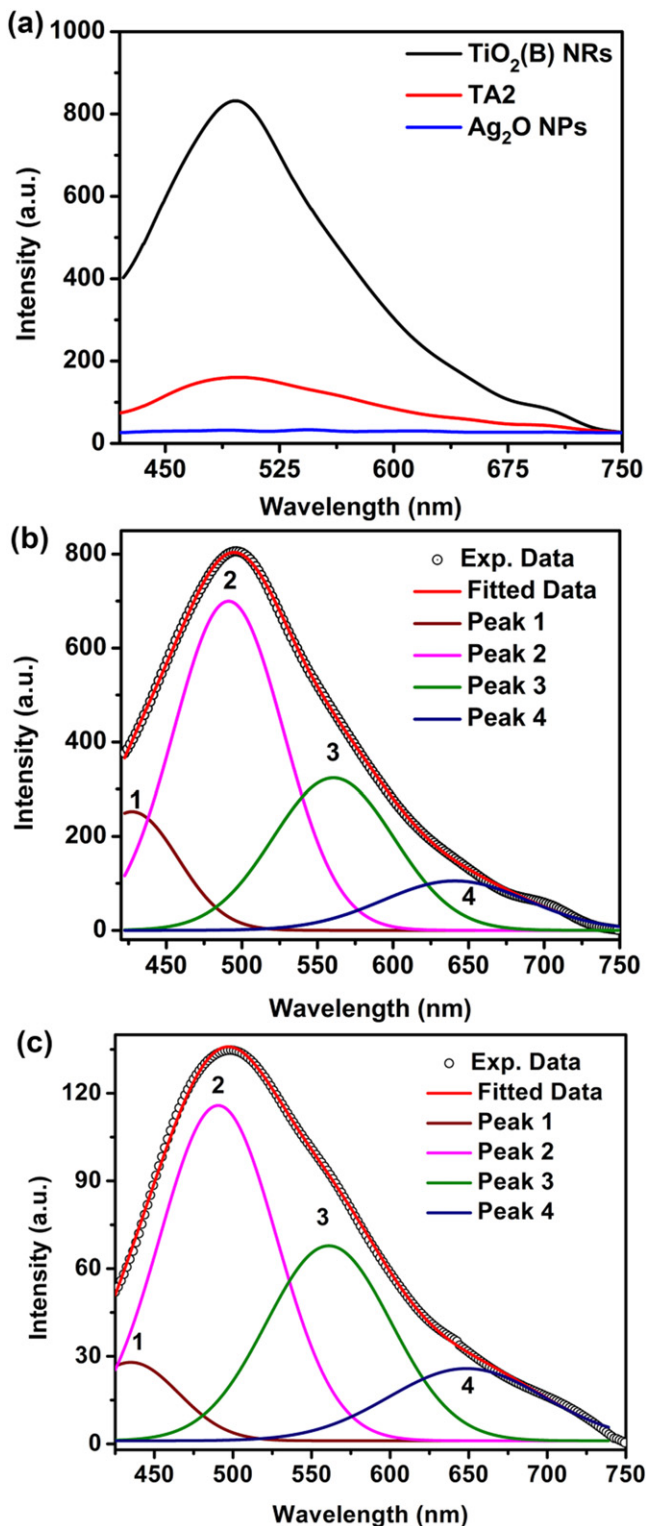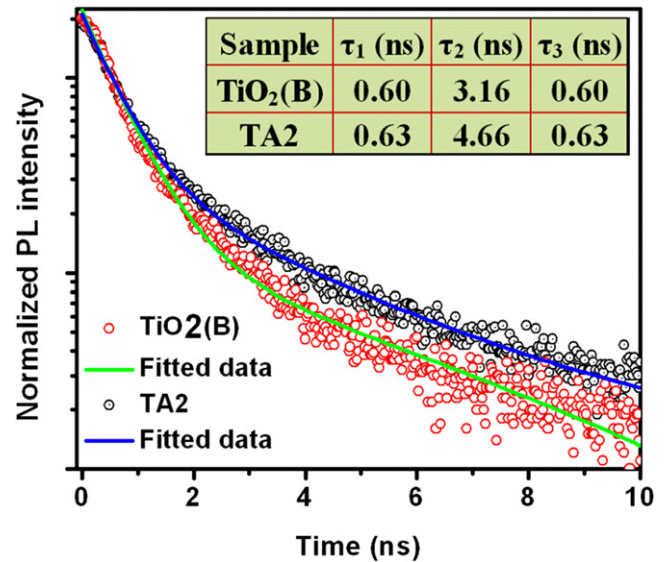
Figure 7. A comparison of the TRPL spectra for TiO$_2$(B) NRs and the TA2 HS monitored at 490 nm (emission) with a 405 nm laser excitation. The symbols represent the experimental data and solid lines represent the corresponding tri-exponential fit. The inset shows the time constants for the different samples.

Figure 6. (a) A comparison of the PL spectra for TiO$_2$(B) NRs, Ag$_2$O NPs and TA2 excited with a 405 nm laser. (b), (c) The Gaussian fitted PL spectra of the TiO$_2$(B) NRs and TA2, respectively.

comparison of the TRPL decay curves for TiO$_2$(B) NRs and TA2 monitored at 490 nm using a laser excitation source (405 nm). Each TRPL spectral data is fitted by a tri-exponential decay function. The corresponding time constants (τ) are tabulated as an inset in figure 7. The tri-exponential fit implies

that three different states contribute to the TRPL spectra in each sample, and this is fully consistent with the steady state PL spectra. The values of τ_1 and τ_3 are quite similar for both the samples. However, τ_2 increases considerably after Ag$_2$O loading, and as a result the decay becomes slower in TA2. The increase in carrier lifetime seems to play a critical role in the enhanced photocatalytic efficiency of the HS samples. The photogenerated charge carriers first migrate to the interface of the TiO$_2$/Ag$_2$O, which is thermodynamically favorable, since the valence and conduction band position of Ag$_2$O is above of that of the TiO$_2$(B) NR [37]. Once the electrons from the valence band to the conduction band are excited, the electrons from the conduction band of the Ag$_2$O NPs migrate to the conduction band of the TiO$_2$(B) NRs and the holes from the valence band of the TiO$_2$(B) NRs migrate to those of the Ag$_2$O NPs. Thus, the interfacial charge transfer prolongs the lifetime of the photogenerated charge carriers, which is clearly manifested as a longer τ in the TRPL spectra. By decorating the Ag$_2$O NPs on TiO$_2$(B) NRs, the probability of recombination decreases and a higher density of carriers is available on the surface of the HS, promoting high visible light photocatalytic performance, as discussed below.

3.5. Photocatalytic studies

The excitons generated within the Ag$_2$O NPs decorated on the TiO$_2$(B) NRs could be energetic enough to drive photoelectrochemical reactions due to the NPs' broadband optical absorption and prolonged carrier lifetime. To investigate the photocatalytic efficiency of the samples, we examined the decomposition of MO and MB in water in the presence of the HS catalysts.
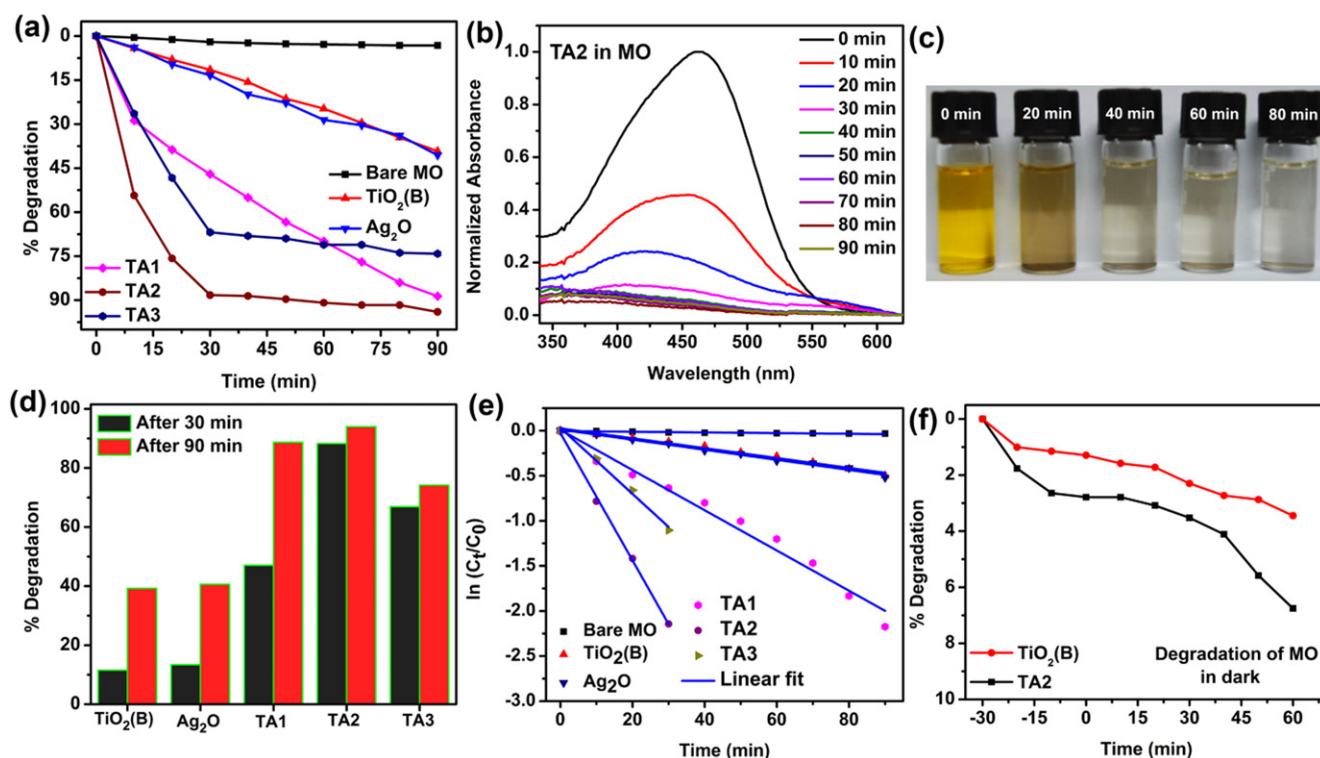
Figure 8. (a) A comparison of the photocatalytic degradation profiles of MO with and without the presence of different catalyst samples under visible light irradiation. (b) Normalized absorption spectra of MO under visible light irradiation catalyzed by the TA2 HS at a regular interval of 10 min. (c) A digital photograph of the degradation color change of MO in the presence of TA2 after exposure to visible light for various times. (d) A comparison of the degradation percentages of MO after 30 and 90 min of irradiation calculated for different samples. (e) A plot of $\ln(C_t/C_0)$ versus exposure time (t) for different samples and the corresponding linear fitting. (f) A comparison of the degradation of MO by the TiO_2 NRs and the TA2 catalysts in the dark.

3.5.1. Photocatalytic degradation of MO. The visible light photocatalytic properties of all the samples were ascertained under identical conditions using an aqueous solution of MO as a reference dye. In order to compare the efficiencies, the self-decomposition of the dye solution was also examined under identical conditions. Figure 8(a) shows a comparison of the photodegradation performance of samples TA1, TA2, TA3 and bare TiO_2(B) NRs under visible light illumination. The photocatalytic degradation of the bare Ag_2O NPs and blank MO is also shown for comparison. The HS samples show enhanced photodegradation efficiency as compared to the bare TiO_2 NRs and bare Ag_2O NPs. Note that among all the HS samples, TA2 shows the highest photodegradation efficiency. Figure 8(b) shows the normalized absorbance of MO aqueous solution collected at a regular time interval (10 min) for sample TA2 under visible light irradiation. The digital photographs of the change in color of the MO solution due to photodegradation at an interval of 20 min for sample TA2 are shown in figure 8(c). Figure 8(d) shows the comparison of the photodegradation efficiency of the samples after 30 min and 90 min light irradiation. The catalysts TA2 and TA3 degrade the dye very rapidly after 30 min of irradiation and then the rate of degradation becomes very slow (figures 8(a) and (d))—as expected for exponential decay kinetics. After 30 min of light irradiation, the MO is decomposed by 88.2% and 66.9% for TA2 and TA3, respectively. The kinetics of the photodegradation of MO

can be described by the pseudo-first-order rate kinetics from the Langmuir–Hinshelwood expression: $\ln(C_t/C_0) = -kt$, where C_0 is the initial concentration of MO after reaching the adsorption–desorption equilibrium, C_t is the concentration of MO after irradiation time t, and k is the rate constant (min^{-1}). Figure 8(e) shows a comparison of the values of $\ln(C_t/C_0)$ for the respective samples as a function of light irradiation time. The rate constant is calculated by the corresponding linear fit and the value of k is tabulated in table 2. Interestingly, k (0.071 min^{-1}) is found to be highest for sample TA2 and is found to be 12.9 fold stronger than that of the TiO_2(B) NRs (0.0055 min^{-1}) or the Ag_2O NPs (0.0056 min^{-1}). Considering the visible light irradiation, the rate constant of 0.071 min^{-1} is very significant for the HS sample. Most of the reported k-values are usually for UV light irradiation and the reported rate constant for a commercial photocatalyst (e.g., P25) is ~1 × 10^{-2} min^{-1} under UV light irradiation [42]. In the present case, even under visible light irradiation, the rate constant is about one order of magnitude higher than the reported values of TiO_2 under UV light irradiation.

In order to understand the degradation efficiency of the TiO_2(B) NR and its HS in the dark, the experiments were performed under the same conditions but in the absence of light. The catalysts were mixed with an aqueous solutions of MO and stirred magnetically in the dark; 5 ml solution was then immediately withdrawn. Then the process was continued for 90 min. We assumed that the adsorption/desorption

Table 2. The degradation performance of organic dyes (MO and MB) by various catalysts and the corresponding pseudo-first-order rate constants.

Catalyst name	Degradation (%)		Rate constant (min^{-1})	
	MO	MB	MO	MB
No catalyst	3.2	9.2	0.000 37	0.001
TiO$_2$(B) NRs	39.2	60.5	0.0055	0.01
Ag$_2$O NPs	40.6	87.9	0.0056	0.021
TA1 HS	88.6	93.5	0.022	0.033
TA2 HS	94	99.2	0.071	0.057
TA3 HS	74.2	97.5	0.037	0.046

equilibrium condition had been reached within 30 min. Beyond the equilibrium condition, the degradation activity of the TiO$_2$(B) NRs and the most efficient photocatalyst TA2 was monitored up to 60 min further; the corresponding degradation results are shown in figure 8(f). The concentration of the dye decreases very marginally with time because of the adsorption of dye molecules on the catalyst surface due to the pores there (as shown in figures 2(a) and (b)). Since due to the adsorption the degradation of the dye is very small (2% for TiO$_2$ NRs and 7% for TA2 after 90 min) as compared to the high degradation in the presence of light, we have not considered the contribution of the adsorption in the calculation of the rate constant.

3.5.2. Photocatalytic degradation of MB. In order to understand the photocatalytic effect of TiO$_2$(B)/Ag$_2$O HSs on a different ionic dye (a cationic instead of an anionic dye, MO), we performed the photocatalytic experiment on methylene blue (MB) under identical conditions to that of the MO. Figure 9(a) shows a comparison of the photodegradation performance of samples TA1, TA2, TA3 and the bare TiO$_2$(B) NRs in the MB aqueous solution. The photocatalytic degradation of blank Ag$_2$O NPs and blank MB are also shown for comparison. Here, again the HS samples show enhanced photodegradation efficiency as compared to the bare TiO$_2$ NRs and Ag$_2$O NPs. As before, sample TA2 shows the highest photodegradation efficiency as compared to the other samples. Figure 9(b) shows the normalized absorbance of the MB aqueous solution collected at a regular interval of 10 min for sample TA2 under visible light irradiation. The digital photographs of the change in color of the MB solution after photodegradation at an interval of 20 min for sample TA2 are shown in figure 9(c). Figure 9(d) shows a comparison of the photodegradation efficiency of the samples after 30 min and 90 min light irradiation. Figure 9(e) shows a comparison of the value of $\ln(C_t/C_0)$ for the respective samples as a function of light irradiation time. The rate constant is calculated by the corresponding linear fit and the value of k is tabulated in table 2. The degradation of the MB solution by the TiO$_2$ NRs and the TA2 HS in the absence of light is shown in figure 9(f). The rate constant in MB (as shown in figure 9(e)) and table 2) for TA2 (0.057 min^{-1}) is the highest, and 5.7 times higher than its value in TiO$_2$(B) NRs (0.01 min^{-1}). In this case, the

enhancement factor (5.7) is less than that of the MO dye (12.9). In both cases, i.e. for the dyes of different ionic nature, the photocatalytic efficiency of the HS samples is strongly enhanced as compared to the bare TiO$_2$ or Ag$_2$O samples, and a detailed mechanism of the enhancement is discussed later.

3.5.3. Cyclic stability of photocatalysis. To investigate the cyclic stability of the TiO$_2$(B)/Ag$_2$O HS as a photocatalyst under visible light irradiation, the same sample was repeatedly used for four cycles after separation by centrifugation followed by filtration. The TA2 HS was chosen as the model HS catalyst because it has the highest photodegradation efficiency, as shown in figures 8 and 9 for MO and MB, respectively. Interestingly, the TA2 photocatalyst exhibits extremely stable photocatalytic activity under visible light irradiation for MO, as shown in figure 10(a), and there is no obvious reduction in photodegradation efficiency after four cycles of use. In the case of MB, TA2 again shows very good stability under a repeated cyclic process, though the degradation rate falls slightly after four cycles (figure 10(b)). Thus, the Ag$_2$O-decorated TiO$_2$(B) NRs are found to be extremely stable photocatalysts with potential for real life applications. The hydrothermal synthesis allows the large scale production of these catalysts at a low cost for their use in commercial applications. Our results have demonstrated the superiority of the TiO$_2$(B)/Ag$_2$O HS over the bare TiO$_2$(B) NRs for advanced applications in environmental cleaning.

3.5.4. Mechanism of enhanced visible light photocatalytic activity. As a bulk crystalline material, TiO$_2$ is a large band gap (3.2 eV) semiconductor, and is optically active only at light irradiation wavelengths shorter than approximately 400 nm. In the present work, the band gap of a pure TiO$_2$ NR and its HS is tuned so that it can sense a broad spectrum of solar light. In the pure TiO$_2$ B-phase, the range of photo activity of TiO$_2$ NRs (band gap 2.8 eV) is enhanced as compared to bulk TiO$_2$, and found to be capable of light absorption up to ~440 nm. Thus under visible light irradiation, pure TiO$_2$(B) NRs show reasonably high photodegradation efficiency (see table 2). Pure Ag$_2$O NPs also show reasonably high visible light photo degradation efficiency, as shown in table 2. When Ag$_2$O NPs are decorated on pure B-phase TiO$_2$ NRs, a massive enhancement in photodegradation efficiency is recorded. Here, the Ag$_2$O NPs might act as a visible light sensitizer leading to enhanced visible light photocatalytic activity. There are several factors that may contribute to this enhancement, such as

  i. Enhanced surface area
 ii. Tunable band gap and enhanced optical absorption range
iii. High adsorption of dye and dye-catalyst interaction
 iv. Efficient charge separation at the interface of the HS
  v. Ionic condition of the dye as well the heterostructure material
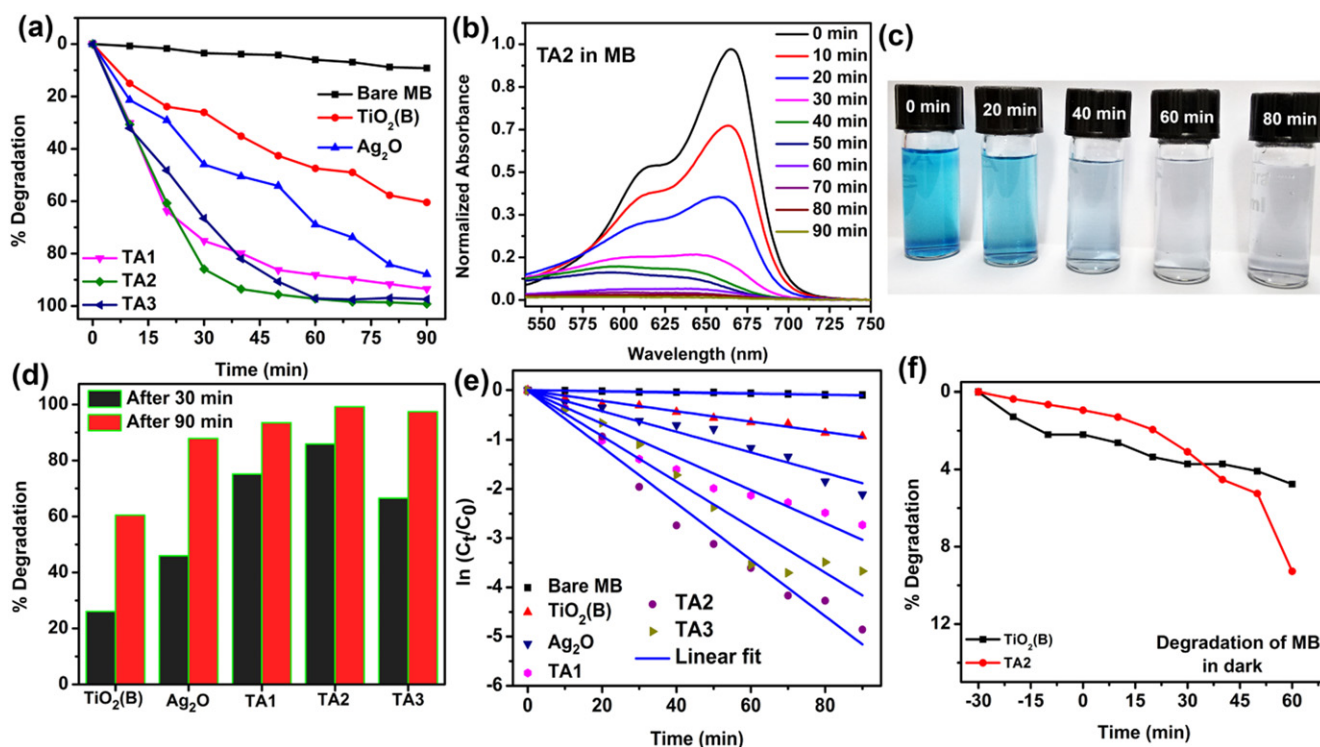
Figure 9. (a) A comparison of the photocatalytic degradation profiles of MB with and without the presence of different catalyst samples under visible light irradiation. (b) The normalized absorption spectra of MB under visible light irradiation catalyzed by TA2 measured at a regular interval of 10 min. (c) A digital photograph of the color change of MB after visible light exposure for different times decomposed by TA2 HS. (d) A comparison of the degradation percentages of MB after 30 and 90 min of irradiation calculated for different samples. (e) $\ln(C_t/C_0)$ versus exposure time (t) plot of different samples and the corresponding linear fitting. (f) A comparison of the degradation of MB by TiO_2 NRs and TA2 catalysts in the dark.

A high surface area is generally desirable for having enhanced photocatalytic activity in a semiconductor photocatalyst, since higher surface areas allow greater interfacial contact points with the organic dyes leading to enhanced photodegradation efficiency. However, in our case, the specific surface area of the $TiO_2(B)$ NRs was reduced after the formation of the HS with the Ag_2O NPs, as confirmed by the BET analysis, although the photodegradation efficiency of the sample TA2 is much higher than the bare $TiO_2(B)$ NRs, as shown in table 2. Thus, it can be concluded that surface area is not the primary factor for the enhanced photocatalytic activity observed here.

The rate of photocatalysis depends on the relative concentration of the dye and the catalyst in the solution. In the present case, a 100 ml dye solution (10 mg l^{-1}) was used with a 20 mg catalyst. Thus, 1 mg dye was degraded by up to 76% within 20 min by 20 mg of TA2 in the presence of visible light. Zhou *et al* have reported the ~77% degradation of MO in 20 min by Ag_2O and an anatase TiO_2 HS with a 1:1 weight ratio [8]. However, the authors only used 0.4 mg MO in the aqueous solution, which is 2.5 times less than the amount that was used in the present study. Thus, in the present case, the fabricated HS shows photocatalysis 2.5 times stronger than that reported earlier using the TiO_2 (anatase)/Ag_2O HS in the presence of visible light.

The photocatalysis process requires the high absorption of light to create enough e–h pairs and easy separation of the

photoexcited e–h pairs with minimum recombination. The band gap of the as-synthesized TiO_2 NRs and the HS samples coupled with the Ag_2O NPs clearly falls in the visible range (in figure 5(b) and table 1) and is likely to be effective for the generation of enough photoexcited carriers. Broad band optical absorption with a high intensity for the HS samples allows the generation of a high density of photoinduced carriers that can facilitate certain redox reactions to degrade the organic pollutants. Sample TA2 shows visible absorption of the highest intensity as compared to the other HS samples, and this also extends to the NIR region, which is possibly one of the important reasons behind it having the highest level of photocatalytic efficiency among all the HS samples.

In a semiconducting material, fast recombination of the photoexcited e–h pairs is mostly observed in the form of PL, and the separation of photoexcited e–h pairs with minimum recombination is highly challenging. Efficient separation of the photogenerated e–h pairs is essential for the generation of highly active superoxide and hydroxyl radicals to facilitate enough redox reaction for the degradation of the dye. On the basis of the above-illustrated enhanced photodegradation by a $TiO_2(B)/Ag_2O$ HS under visible light irradiation, the following mechanism can be proposed. A possible band diagram of the $TiO_2(B)Ag_2O$ HS at the interface as well as the carrier transfer mechanism are schematically illustrated in figure 11. In the HS, Ag_2O NPs are well coupled to the $TiO_2(B)$ NRs, and the energy bands of the Ag_2O and $TiO_2(B)$

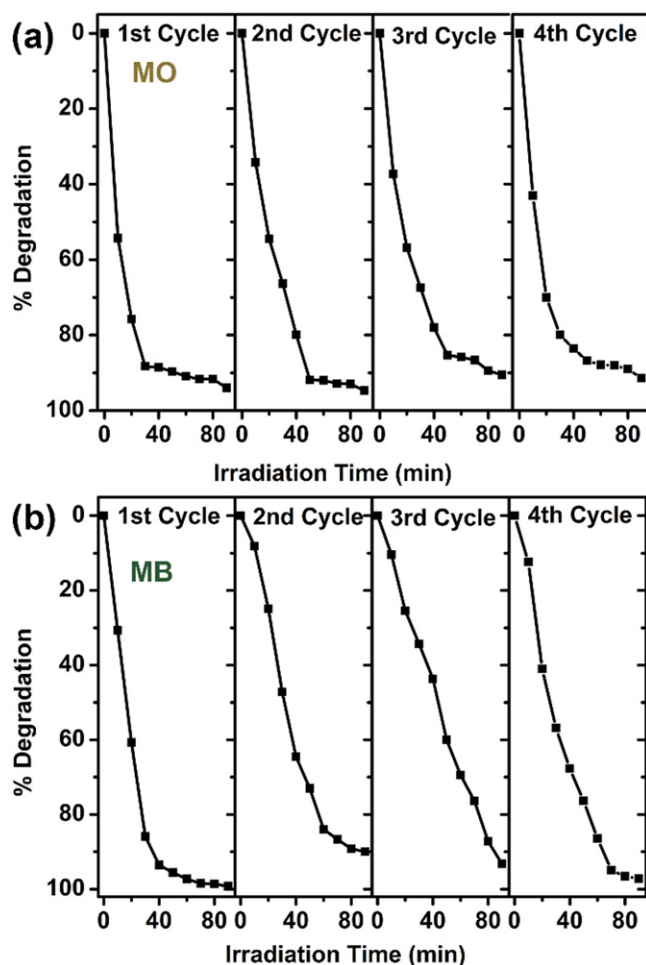**Figure 10.** The cyclic stability of the TA2 HS as a visible light photocatalyst for four cycles: (a) in MO and (b) in MB.

process promotes the longer lifetime of the charge carriers reducing their recombination probability, which is consistent with the TRPL results. Adsorbed O_2 and H_2O molecules react with the photogenerated electrons at the interface of the HS to form superoxide radicals, and holes can be trapped by the hydroxyl groups to form hydroxyl radicals. Thus, a sufficient number of powerful super oxide and hydroxyl radicals are generated and they decompose the adsorbed organic pollutants. The reaction mechanism goes as follows [8]:

1. $TiO_2(B) \xrightarrow{h\nu} e^- + h^+$
2. $Ag_2O \xrightarrow{h\nu} e^- + h^+$
3. $O_2 \text{ (at interface)} + e^- \rightarrow \bullet O_2^-$
4. $H_2O \rightarrow H^+ + OH^-$
5. $OH^- + h^+ \rightarrow \bullet OH$
6. $\text{Organic dye} + \bullet OH \rightarrow \text{degradation products}$
7. $\text{Organic dye} + \bullet O_2^- \rightarrow \text{degradation products}$

However, under visible light illumination holes accumulate on the Ag_2O surface by transferring electrons to the $TiO_2(B)$ surface. Thus, the $TiO_2(B)$ becomes anionic by gathering electrons and Ag_2O becomes cationic in nature by accumulating holes. In the HS, the Ag_2O NPs are uniformly coated on the $TiO_2(B)$ surface and the HS as a whole behaves in a cationic nature from the surface. As the dye MO is anionic in nature, in an aqueous solution the anionic dye radicals feel columbic attraction to the cations (h^+) on the HS surface. Thus, the anionic dye radicals get adsorbed very easily into the HS surface and react easily with the hydroxyl radicals (step 6). As the hydroxyl radicals are mainly generated at the Ag_2O surface, concentration of this radical is very high here. Thus, MO gets decomposed very rapidly with time under visible light irradiation. Note that MB is slightly cationic in nature. So, in an aqueous solution there is columbic repulsion between the cationic MB radicals and cationic Ag_2O surface in the HS samples. Thus, the adsorption rate of MB dye radicals at the HS surface is slower than that of the MO radicals, which results in the slower degradation of MB, as shown in table 2 [45]. Nevertheless, the degradation rate is considerably high due to the high density of photoinduced carriers present in the HSs resulting in the significant degradation of MB by the superoxide and hydroxyl radicals. Thus, $TiO_2(B)/Ag_2O$ HSs are capable of the degradation of both anionic and cationic dyes.

4. Conclusions

A nanoporous $TiO_2(B)/Ag_2O$ NR HS has been successfully fabricated by a low-temperature hydrothermal method followed by a co-precipitation method, and the HS is shown to be highly efficient in the visible light photodegradation of both anionic and cationic organic dyes. The morphology, structure, phase and elemental composition of the individual component and the HS have been studied by FESEM, TEM, XRD, XPS and EDX. DRS, PL and TRPL studies helped us to understand the optical properties of the systems and explain

are aligned suitably to facilitate charge transfer. Previous reports suggest that in the $TiO_2(B)/Ag_2O$ HSs, both the CB and the VB of the Ag_2O NPs lie above the corresponding bands of the $TiO_2(B)$ [37, 43]. Therefore, the migration of the photogenerated charge carriers through the interface of the HS is thermodynamically favorable [37]. The decrease in the PL intensity of TiO_2 NRs and the slower decay rate in the TRPL after the Ag_2O NPs have been loaded onto it, strongly suggest that efficient charge separation indeed takes place in the HS samples. The photogenerated electrons and holes react with the adsorbed O_2 and H_2O molecules, respectively, to form superoxide radicals and hydroxyl radicals. The resulting hydroxyl radical, being a strong oxidizing agent, and the super oxide radicals, a strong reducing agent, can degrade most of the organic dyes to the end products. Ag_2O NPs are fully visible light sensitive due to their narrow band gap (1.34 eV). When the $TiO_2(B)$ NRs and Ag_2O NPs are exposed as HSs to the visible light, both the components produce electrons in the conduction band leaving behind holes in the valence band. Due to the band positions and their bending [44], photoexcited electrons from the CB of the Ag_2O migrate to that of the TiO_2 and holes from the VB of the TiO_2 move to those of the Ag_2O. This charge transfer

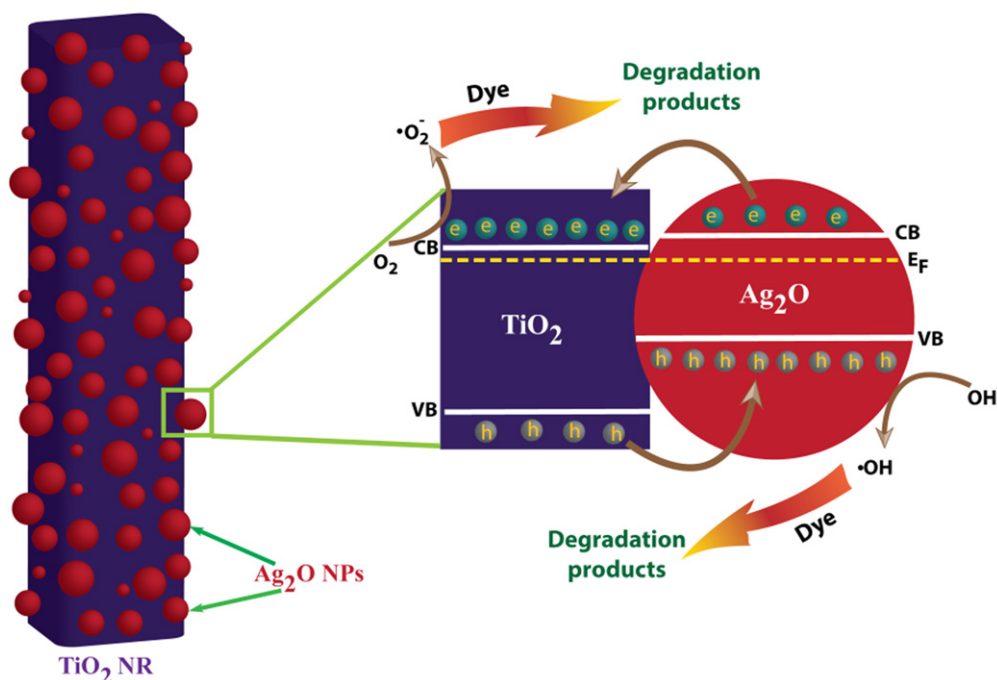**Figure 11.** A schematic representation of the $TiO_2(B)/Ag_2O$ NR HS and the corresponding band alignment at the interface showing the charge separation and the corresponding photodegradation mechanism.

the mechanism behind efficient visible light photocatalysis. Ag_2O NPs act as a photosensitizer enabling the $TiO_2(B)$ NRs to be highly active in the visible region. The thermodynamically favored band structure of the nanocomposite ensures efficient charge separation, prolonging the lifetime of the photogenerated charge carriers that causes enhanced as well as stable visible light photodegradation activity. Our results demonstrate that $TiO_2(B)/Ag_2O$ NR HSs are efficient in the degradation of both anionic and cationic dyes. The photocatalytic efficiency and the degradation rate of $TiO_2(B)/Ag_2O$ are maximum for a 1:1 weight ratio of $TiO_2(B):Ag_2O$ in both MO and MB. We achieved a pseudo-first-order rate constant of 0.071 min^{-1}, which is four times higher than the reported values. These HS photocatalysts are shown to be very stable up to four cycles of catalysis. Thus, semiconductor photocatalysts incorporated with metal oxide NPs, such as Ag_2O, CuO, PdO, NiO, Ag_2CO_3 could help to enhance visible light sensitization and efficient charge transfer at the interface leading to improved solar-light-driven photocatalysis. These results are significant for the advanced energy and environmental applications of metal oxide nanostructures and their heterostructures.

Acknowledgments

References

[1] Kazuhito H, Hiroshi I and Akira F 2005 TiO_2 photocatalysis: a historical overview and future prospects *Japan. J. Appl. Phys.* **44** 8269

[2] Fox M A and Dulay M T 1993 Heterogeneous photocatalysis *Chem. Rev.* **93** 341

[3] Hoffmann M R, Martin S T, Choi W and Bahnemann D W 1995 Environmental applications of semiconductor photocatalysis *Chem. Rev.* **95** 69

[4] Liu L, Zhao H, Andino J M and Li Y 2012 Photocatalytic CO_2 reduction with H_2O on TiO_2 nanocrystals: comparison of anatase, rutile, and brookite polymorphs and exploration of surface chemistry *ACS Catal.* **2** 1817

[5] Liang Y-C, Wang C-C, Kei C-C, Hsueh Y-C, Cho W-H and Perng T-P 2011 Photocatalysis of Ag-loaded TiO_2 nanotube arrays formed by atomic layer deposition *J. Phys. Chem. C* **115** 9498

[6] Chen L, Chen F, Shi Y and Zhang J 2012 Preparation and visible light photocatalytic activity of a graphite-like carbonaceous surface modified TiO_2 photocatalyst *J. Phys. Chem. C* **116** 8579

[7] Zhang H, Lv X, Li Y, Wang Y and Li J 2010 P25-graphene composite as a high performance photocatalyst *ACS Nano* **4** 380

[8] Zhou W, Liu H, Wang J, Liu D, Du G and Cui J 2010 Ag_2O/TiO_2 nanobelts heterostructure with enhanced ultraviolet and visible photocatalytic activity *ACS Appl. Mater. Interfaces* **2** 2385

[9] Xuming Z, Yu Lim C, Ru-Shi L and Din Ping T 2013 Plasmonic photocatalysis *Rep. Prog. Phys.* **76** 046401

[10] Schneider J, Matsuoka M, Takeuchi M, Zhang J, Horiuchi Y, Anpo M and Bahnemann D W 2014 Understanding TiO_2 photocatalysis: mechanisms and materials *Chem. Rev.* **114** 9919

[11] Tanaka A, Ogino A, Iwaki M, Hashimoto K, Ohnuma A, Amano F, Ohtani B and Kominami H 2012 Gold–titanium (IV) oxide plasmonic photocatalysts prepared by a colloid-photodeposition method: correlation between physical properties and photocatalytic activities *Langmuir* **28** 13105

[12] Zhao W, Feng L, Yang R, Zheng J and Li X 2011 Synthesis, characterization, and photocatalytic properties of Ag modified hollow SiO_2/TiO_2 hybrid microspheres *Appl. Catal.* B **103** 181

[13] He X, Cai Y, Zhang H and Liang C 2011 Photocatalytic degradation of organic pollutants with Ag decorated free-standing TiO_2 nanotube arrays and interface electrochemical response *J. Mater. Chem.* **21** 475

[14] Zhou W, Du G, Hu P, Li G, Wang D, Liu H, Wang J, Boughton R I, Liu D and Jiang H 2011 Nanoheterostructures on TiO_2 nanobelts achieved by acid hydrothermal method with enhanced photocatalytic and gas sensitive performance *J. Phys. Chem.* **21** 7937

[15] Kochuveedu S T, Kim D-P and Kim D H 2012 Surface-plasmon-induced visible light photocatalytic activity of TiO_2 nanospheres decorated by Au nanoparticles with controlled configuration *J. Phys. Chem.* C **116** 2500

[16] DuChene J S, Sweeny B C, Johnston-Peck A C, Su D, Stach E A and Wei W D 2014 Prolonged hot electron dynamics in plasmonic-metal/semiconductor heterostructures with implications for solar photocatalysis *Angew. Chem. Int. Ed.* **53** 7887

[17] Ma X-C, Dai Y, Yu L and Huang B-B 2016 Energy transfer in plasmonic photocatalytic composites *Light Sci. Appl.* **5** e16017

[18] Ma X, Dai Y, Yu L and Huang B 2014 New basic insights into the low hot electron injection efficiency of gold-nanoparticle-photosensitized titanium dioxide *ACS Appl. Mater. Interfaces* **6** 12388

[19] Hu C, Hu X, Wang L, Qu J and Wang A 2006 Visible-light-induced photocatalytic degradation of azodyes in aqueous AgI/TiO_2 dispersion *Environ. Sci. Technol.* **40** 7903

[20] Tian J *et al* 2013 Enhanced Photocatalytic Performances of CeO2/TiO_2 nanobelt heterostructures *Small* **9** 3864

[21] Sun J, Li X, Zhao Q, Ke J and Zhang D 2014 Novel V2O5/BiVO4/TiO_2 nanocomposites with high visible-light-induced photocatalytic activity for the degradation of toluene *J. Phys. Chem.* C **118** 10113

[22] Choi W, Termin A and Hoffmann M R 1994 The role of metal ion dopants in quantum-sized TiO_2: correlation between photoreactivity and charge carrier recombination dynamics *J. Phys. Chem.* **98** 13669

[23] He Z, Xie L, Tu J, Song S, Liu W, Liu Z, Fan J, Liu Q and Chen J 2010 Visible light-induced degradation of phenol over iodine-doped titanium dioxide modified with platinum: role of platinum and the reaction mechanism *J. Phys. Chem.* C **114** 526

[24] Wang J, Tafen D N, Lewis J P, Hong Z, Manivannan A, Zhi M, Li M and Wu N 2009 Origin of photocatalytic activity of nitrogen-doped TiO_2 nanobelts *J. Am. Chem. Soc.* **131** 12290

[25] Naldoni A, Allieta M, Santangelo S, Marelli M, Fabbri F, Cappelli S, Bianchi C L, Psaro R and Dal Santo V 2012 Effect of nature and location of defects on bandgap narrowing in black TiO_2 nanoparticles *J. Am. Chem. Soc.* **134** 7600

[26] Santara B, Giri P K, Imakita K and Fujii M 2013 Evidence for Ti interstitial induced extended visible absorption and near infrared photoluminescence from undoped TiO_2 nanoribbons: an *in situ* photoluminescence study *J. Phys. Chem.* C **117** 23402

[27] Kong M, Li Y, Chen X, Tian T, Fang P, Zheng F and Zhao X 2011 Tuning the relative concentration ratio of bulk defects to surface defects in TiO_2 nanocrystals leads to high photocatalytic efficiency *J. Am. Chem. Soc.* **133** 16414

[28] Jiang T, Jia C, Zhang L, He S, Sang Y, Li H, Li Y, Xu X and Liu H 2015 Gold and gold-palladium alloy nanoparticles on heterostructured TiO_2 nanobelts as plasmonic photocatalysts for benzyl alcohol oxidation *Nanoscale* **7** 209

[29] Blumberg I, Starosvetsky J, Bilanovic D and Armon R 2009 TiO_2 P-25 anatase rapid precipitation from water by use of struvite formation *J. Colloid Interface Sci.* **336** 107

[30] Zhou W J, Leng Y H, Hou D M, Li H D, Li L G, Li G Q, Liu H and Chen S W 2014 Phase transformation and enhanced photocatalytic activity of S-doped Ag_2O/TiO_2 heterostructured nanobelts *Nanoscale* **6** 4698

[31] Ghosh R, Imakita K, Fujii M and Giri P K 2016 Effect of Ag/Au bilayer assisted etching on the strongly enhanced photoluminescence and visible light photocatalysis by Si nanowire arrays *Phys. Chem. Chem. Phys.* **18** 7715

[32] Santara B, Giri P K, Imakita K and Fujii M 2013 Evidence of oxygen vacancy induced room temperature ferromagnetism in solvothermally synthesized undoped TiO_2 nanoribbons *Nanoscale* **5** 5476

[33] Waterhouse G I N, Bowmaker G A and Metson J B 2001 The thermal decomposition of silver (I, III) oxide: a combined XRD, FT-IR and Raman spectroscopic study *Phys. Chem. Chem. Phys.* **3** 3838

[34] Murray B J, Li Q, Newberg J T, Menke E J, Hemminger J C and Penner R M 2005 Shape- and size-selective electrochemical synthesis of dispersed silver(I) oxide colloids *Nano Lett.* **5** 2319

[35] Batakrushna S, Giri P K, Kenji I and Minoru F 2014 Microscopic origin of lattice contraction and expansion in undoped rutile TiO_2 nanostructures *J. Phys. D: Appl. Phys.* **47** 215302

[36] Neimark A V, Lin Y, Ravikovitch P I and Thommes M 2009 Quenched solid density functional theory and pore size analysis of micro-mesoporous carbons *Carbon* **47** 1617

[37] Wang Y, Liu L, Xu L, Cao X, Li X, Huang Y, Meng C, Wang Z and Zhu W 2014 Ag_2O/TiO_2/V2O5 one-dimensional nanoheterostructures for superior solar light photocatalytic activity *Nanoscale* **6** 6790

[38] Ramakrishnan R, Devaki S J, Aashish A, Thomas S, Varma M R and Kpp N 2016 Nanostructured semiconducting PEDOT–TiO_2/ZnO hybrid composites for nanodevice applications *J. Phys. Chem.* C **120** 4199

[39] Choudhury B, Bayan S, Choudhury A and Chakraborty P 2016 Narrowing of band gap and effective charge carrier separation in oxygen deficient TiO_2 nanotubes with improved visible light photocatalytic activity *J. Colloid Interface Sci.* **465** 1

[40] Yang M, Liu W, Sun J-L and Zhu J-L 2012 High magnetic field annealing effect on visible photoluminescence enhancement of TiO_2 nanotube arrays *Appl. Phys. Lett.* **100** 043106

[41] Choudhury B, Dey M and Choudhury A 2013 Shallow and deep trap emission and luminescence quenching of TiO_2 nanoparticles on Cu doping *Appl. Nanosci.* **4** 499

[42] Shao X, Lu W, Zhang R and Pan F 2013 Enhanced photocatalytic activity of TiO_2-C hybrid aerogels for methylene blue degradation *Sci. Rep.* **3** 3018

[43] Hoflund G B, Hazos Z F and Salaita G N 2000 Surface characterization study of Ag, AgO, and Ag_2O using x-ray photoelectron spectroscopy and electron energy-loss spectroscopy *Phys. Rev.* B **62** 11126–33

[44] Sarkar D, Ghosh C K, Mukherjee S and Chattopadhyay K K 2013 Three dimensional Ag_2O/TiO_2 type-II (p–n) nanoheterojunctions for superior photocatalytic activity *ACS Appl. Mater. Interfaces* **5** 331

[45] Konstantinou I K and Albanis T A 2004 TiO_2-assisted photocatalytic degradation of azo dyes in aqueous solution: kinetic and mechanistic investigations: a review *Appl. Catal.* B **49** 1